

RESEARCH ARTICLE | JANUARY 17 2024

## Open-boundary cluster model with a parameter-free complex absorbing potential

Kosuke Imamura ; Tomokazu Yasuike ; Hirofumi Sato  



*J. Chem. Phys.* 160, 034103 (2024)

<https://doi.org/10.1063/5.0184571>



View  
Online



Export  
Citation

CrossMark



**Chemical Physics Reviews**

**Special Topic: AI and Machine Learning  
in Chemical and Materials Science**

**Submit Today**



# Open-boundary cluster model with a parameter-free complex absorbing potential

Cite as: J. Chem. Phys. 160, 034103 (2024); doi: 10.1063/5.0184571

Submitted: 26 October 2023 • Accepted: 22 December 2023 •

Published Online: 17 January 2024



View Online



Export Citation



CrossMark

Kosuke Imamura,<sup>1</sup>  Tomokazu Yasuike,<sup>2,a)</sup>  and Hirofumi Sato<sup>1,3,b)</sup> 

## AFFILIATIONS

<sup>1</sup>Department of Molecular Engineering, Graduate School of Engineering, Kyoto University, Kyoto 615-8510, Japan

<sup>2</sup>Department of Liberal Arts, Faculty of Liberal Arts, The Open University of Japan, Chiba 261-8586, Japan

<sup>3</sup>Fukui Institute for Fundamental Chemistry, Kyoto University, Kyoto 606-8103, Japan

<sup>a)</sup>Electronic mail: [yasuike@ouj.ac.jp](mailto:yasuike@ouj.ac.jp)

<sup>b)</sup>Author to whom correspondence should be addressed: [hirofumi@moleng.kyoto-u.ac.jp](mailto:hirofumi@moleng.kyoto-u.ac.jp)

## ABSTRACT

In quantum chemical calculations of heterogeneous structures in solids, e.g., when an impurity is located on the surface, the conventional cluster model is insufficient to describe the electronic structure of substrates due to its finite size. The open-boundary cluster model (OCM) overcomes this problem by performing cluster calculations under the outgoing-wave boundary condition. In this method, a complex absorbing potential (CAP) is used to impose the boundary condition, but the CAP used in the previous studies required parameter optimization based on the complex variational principle. This study proposes and applies a parameter-free CAP to OCM calculations. This approach makes it possible to uniquely determine the band-specific CAP based on the surface Green's function theory. Using this CAP, we conducted OCM calculations of the tight-binding model of a one-dimensional semi-infinite chain, and we found that the calculated density of states agreed with the exact one. Surface states of the Newns–Anderson–Grimley model were also computed using the CAP, and the projected density of states on the adsorbed atom was successfully reproduced.

Published under an exclusive license by AIP Publishing. <https://doi.org/10.1063/5.0184571>

## I. INTRODUCTION

Electronic structure calculations for heterogeneous structures in solids are challenging topics in theoretical chemistry.<sup>1–4</sup> Such systems are commonly found in the development of new materials involving chemical substitutions for periodic carbon materials<sup>5</sup> and impurities in solids.<sup>6</sup> In contrast to homogeneous structures such as perfect crystals, typically managed with periodic boundary conditions, the impurity or embedded molecule breaks the translational symmetry, introducing heterogeneity. The challenge of handling such systems arises from the coexistence of localized electronic states corresponding to the impurity or molecule and delocalized states spreading over the solid.

Two primary approaches are employed to describe the electronic structure of such systems. One approach is the cluster model. A subsystem is defined where the target molecule and its surrounding atoms are extracted from the solid, and quantum chemical

calculations are performed on this subsystem. Another approach is the supercell method, which performs band calculations by defining the subsystem as the unit cell. The former is well-suited for describing the heterogeneous, local electronic structure of the target molecule. However, due to the finite size of the cluster, edge effects occur, and the continuous nature of the solid electronic structure is lost. Various studies have been conducted to address these limitations. The simplest example is a model where the solid is represented by a set of point charges, and the cluster is embedded in the electrostatic field generated by them.<sup>7–9</sup> A similar approach is the solid-state quantum mechanics/molecular mechanics (QM/MM) method, which can be applied when the interaction between the cluster and the solid has a covalent nature.<sup>10,11</sup> These classical embedding methods allow us to calculate ionic crystals, oxides, and porous materials such as zeolites and metal organic frameworks (MOFs). If the solid is a metal or an accurate interaction between the cluster and the solid needs to be considered,

the quantum embedding method is required.<sup>12,13</sup> The supercell approach is well-suited for describing electronic states of solids, but it is difficult to describe localized electronic structures, such as locally excited states in a molecule. Additionally, the cell size must be large enough to reduce the intermolecular interactions between neighboring supercells, thereby increasing the computational cost.

The open-boundary cluster model (OCM) overcomes the limitations of the cluster model from a different standpoint.<sup>14–17</sup> In OCM, the cluster calculation under the outgoing wave boundary condition is performed. With this modification, the resulting energy eigenvalues become complex numbers with negative imaginary parts, known as the Siegert eigenvalues.<sup>18</sup> Such a state represents a finite-lived resonance state because the amplitude of the wave function decays exponentially over time. For example, the time evolution of the wave function and amplitude of a state with a complex energy  $E - i\Gamma/2$  ( $\Gamma > 0$ ) is expressed as follows:

$$\Psi(t) = e^{-i(E-i\Gamma/2)t}\Psi(0), \quad (1)$$

$$|\Psi(t)|^2 = e^{-\Gamma t}|\Psi(0)|^2. \quad (2)$$

The inverse of the imaginary part,  $1/\Gamma$ , corresponds to the lifetime of the state. In the conventional cluster model, the electrons are always bounded to the cluster region carved out of the total system. This treatment is obviously unphysical because, in reality, the electrons in the model cluster are expected to diffuse into the entire system. Contrastingly, the resonance states in the OCM calculation mimic these effects adequately. It is noted that a model based on non-Hermitian quantum mechanics has also been developed to deal with these states.<sup>19</sup> Additionally, several studies have calculated the electron injection rate in dye-sensitized materials by modeling the electron transfer from the dye to the substrate as a resonance decay.<sup>20–22</sup> OCM was initially applied to a model system of a one-dimensional solid, demonstrating its ability to reproduce the density of states (DOS) of a solid and provide information on the electron transfer process between the adsorbate and surface.<sup>14</sup> Photo-excited nuclear dynamics was then investigated in the framework of OCM with a model potential for an NO molecule on a Pt(111) surface.<sup>15,16</sup> OCM has also been applied to the first-principles electronic structure calculations, where absorption spectra and excited-state lifetimes of a Cs atom on copper substrates have been calculated.<sup>17</sup>

While OCM successfully described surface phenomena that have been difficult to handle with conventional cluster models, there remains a problem in constructing the complex absorption potential (CAP) to impose the outgoing-wave boundary condition in the calculation. Various CAPs, such as box type<sup>23</sup> and Voronoi type,<sup>24</sup> have been employed in quantum chemical calculations of resonance states. A transmission-free CAP<sup>25</sup> was used in the previous OCM calculation. However, several problems exist in applying these CAPs to OCM calculations. They have in common that the single parameter in the CAP is adjusted based on the complex variational principle<sup>26</sup> to obtain the optimal CAP. This approach does not always yield resonance states because non-physical stationary points sometimes appear.<sup>27</sup> It is also known that the value of the complex energy is sensitive to the position and shape of the CAP.<sup>28</sup> For these reasons, a parameter-free CAP is considered desirable. Moreover, it is worthwhile to be aware that they are state-specific CAPs

because the complex variational principle is applied to a single state or a single orbital energy. This aspect is problematic when we need a band-specific CAP optimized for all the orbitals constituting the solid band.

In this study, we propose a novel method for constructing a parameter-free CAP for OCM calculations. Henderson *et al.* developed a parameter-free CAP based on electron self-energy,<sup>29</sup> overcoming all the problems mentioned earlier. However, their symmetrized CAP was not suitable because the exact eigenvalues from adiabatically connected states were not reproduced. We propose a new symmetrization scheme and find that the resulting OCM calculations with the CAP reproduce well the DOS of solids and the projected DOS (PDOS) of adsorbed atoms. Theoretical details are presented in the next section. The results of applying the developed method to a one-dimensional solid tight-binding model will then be presented.

## II. THEORY

In order to construct a CAP, we follow the approach by Henderson *et al.*<sup>29</sup> Suppose we have a cluster Hamiltonian  $\mathbf{H}$  and energy-dependent self-energy  $\Sigma(\epsilon)$  matrices with sizes of  $N \times N$ . The eigenvalue equation with self-energy is written by

$$[\mathbf{H} + \Sigma(\epsilon_m)]\mathbf{u}_m = \epsilon_m\mathbf{u}_m, \quad (3)$$

$$\mathbf{v}_m^\dagger[\mathbf{H} + \Sigma(\epsilon_m)] = \mathbf{v}_m^\dagger\epsilon_m, \quad (4)$$

where  $\mathbf{u}_m$  and  $\mathbf{v}_m$  are right and left column eigenvectors, respectively. The dagger symbol ( $\dagger$ ) means the Hermitian transpose, and the complex conjugate is denoted by the asterisk symbol ( $*$ ) in this paper.

It is difficult to find resonance states associated with the bound states of the cluster Hamiltonian because there are many other solutions representing continuum states. Adiabatically connected resonance states are thus obtained by solving the following equation:

$$[\mathbf{H} + \lambda\Sigma(\epsilon_m^\lambda)]\mathbf{u}_m^\lambda = \epsilon_m^\lambda\mathbf{u}_m^\lambda, \quad (5)$$

$$\mathbf{v}_m^{\lambda\dagger}[\mathbf{H} + \lambda\Sigma(\epsilon_m^\lambda)] = \mathbf{v}_m^{\lambda\dagger}\epsilon_m^\lambda. \quad (6)$$

The parameter  $\lambda$  is varied gradually from 0 to 1, meaning that the total Hamiltonian adiabatically changes from that of the bare cluster to that of the cluster interacting with solids. The following matrices are then constructed by collecting the eigenvalues and right/left eigenvectors at  $\lambda = 1$ :

$$\epsilon_1 \equiv \text{diag}(\epsilon_1^{\lambda=1}, \dots, \epsilon_N^{\lambda=1}), \quad (7)$$

$$\mathbf{U}_1 \equiv (\mathbf{u}_1^{\lambda=1}, \dots, \mathbf{u}_N^{\lambda=1}), \quad (8)$$

$$\mathbf{V}_1 \equiv (\mathbf{v}_1^{\lambda=1}, \dots, \mathbf{v}_N^{\lambda=1}). \quad (9)$$

We can obtain approximate expressions  $\mathbf{W}^{R/L}$  for the self-energy, which satisfy the following equations:

$$[\mathbf{H} + \mathbf{W}^R]\mathbf{U}_1 = \mathbf{U}_1\epsilon_1, \quad (10)$$

$$\mathbf{V}_1^\dagger[\mathbf{H} + \mathbf{W}^L] = \epsilon_1 \mathbf{V}_1^\dagger. \quad (11)$$

By multiplying the inverse matrices of  $\mathbf{U}_1$  or  $\mathbf{V}_1^\dagger$ , we can obtain the energy-independent CAPs as

$$\mathbf{W}^R = \mathbf{U}_1 \epsilon_1 \mathbf{U}_1^{-1}, \quad (12)$$

$$\mathbf{W}^L = (\mathbf{V}_1^\dagger)^{-1} \epsilon_1 \mathbf{V}_1^\dagger. \quad (13)$$

In this study, we propose a new formalism for symmetrizing Eqs. (12) and (13). As stated in the previous work,<sup>29</sup>  $\mathbf{W}^R$  and  $\mathbf{W}^L$  are not complex-symmetric matrices, and these can be symmetrized by the following equation:<sup>29</sup>

$$\overline{\mathbf{W}} = \frac{\mathbf{W}^R + \mathbf{W}^L}{2}. \quad (14)$$

The overline means that the CAP is symmetrized. However, it is known that this CAP reproduces neither the eigenvalue matrix  $\epsilon_1$  nor the eigenvector matrices  $\mathbf{U}_1, \mathbf{V}_1$  constructed from the adiabatically connected solutions.<sup>29</sup>

Here, the iterative scheme is introduced to reproduce the eigenvalue matrix  $\epsilon_1$ . After the  $k$ th iteration, the symmetrized CAP is defined as

$$\overline{\mathbf{W}}_k = \frac{\mathbf{W}_k^R + \mathbf{W}_k^L}{2}. \quad (15)$$

The initial CAP of the iteration ( $k = 1$ ) is borrowed from Henderson's symmetrized CAP,

$$\mathbf{W}_1^{R/L} \equiv \mathbf{W}^{R/L}, \quad (16)$$

$$\overline{\mathbf{W}}_1 \equiv \overline{\mathbf{W}}. \quad (17)$$

With this CAP, the complex valued eigenvalues and eigenvectors are obtained by solving

$$[\mathbf{H} + \overline{\mathbf{W}}_k] \mathbf{U}_{k+1} = \mathbf{U}_{k+1} \epsilon_{k+1}, \quad (18)$$

$$\mathbf{V}_{k+1}^\dagger [\mathbf{H} + \overline{\mathbf{W}}_k] = \epsilon_{k+1} \mathbf{V}_{k+1}^\dagger. \quad (19)$$

If the absolute difference  $|\epsilon_{k+1} - \epsilon_1|$  is smaller than the specified threshold, the iteration stops, and we can obtain the optimized CAP  $\overline{\mathbf{W}}^{\text{opt}}$  as  $\overline{\mathbf{W}}_k$ . If the convergence is not met, the next step is to obtain the right/left CAPs by

$$\mathbf{W}_{k+1}^R = \mathbf{U}_{k+1} \epsilon_1 \mathbf{U}_{k+1}^{-1}, \quad (20)$$

$$\mathbf{W}_{k+1}^L = (\mathbf{V}_{k+1}^\dagger)^{-1} \epsilon_1 \mathbf{V}_{k+1}^\dagger, \quad (21)$$

so that  $\epsilon_{k+2}$  approaches  $\epsilon_1$ . It is noted that these expressions contain not  $\epsilon_{k+1}$  but  $\epsilon_1$ , although  $\mathbf{U}_{k+1}$  and  $\mathbf{V}_{k+1}$  are used. With these right/left CAPs, the symmetrized CAP is again calculated by Eq. (15), and the next iteration starts.

We perform OCM calculations with the constructed CAP as follows:

$$\begin{aligned} [\mathbf{H} + \overline{\mathbf{W}}^{\text{opt}}] \mathbf{u}_m &= \epsilon_m \mathbf{u}_m, \\ &= (\omega_m - i\gamma_m) \mathbf{u}_m, \end{aligned} \quad (22)$$

where  $\omega_m$  is the real part of the eigenvalue  $\epsilon_m$ , and  $\gamma_m$  is the negative imaginary part of it. Since the CAP is symmetrized, the relationship  $\mathbf{u}_m = \mathbf{v}_m^*$  holds. The (scaled) density of states is represented by the superposition of Lorentz functions whose center and width are characterized by  $\omega_m$  and  $\gamma_m$ , respectively,

$$\rho(E) = \frac{1}{N} \frac{1}{\pi} \sum_{m=1}^N \frac{\gamma_m}{(E - \omega_m)^2 + \gamma_m^2}. \quad (23)$$

The projected density of states on the  $i$ th site can also be expressed analytically

$$\rho_{ii}(E) = -\frac{1}{\pi} \sum_{m=1}^N \frac{\text{Im} \left[ \frac{[\mathbf{u}_m \mathbf{u}_m^T]_{ii} (E - \omega_m - i\gamma_m)}{\mathbf{u}_m^T \mathbf{u}_m (E - \omega_m)^2 + \gamma_m^2} \right]}{(E - \omega_m)^2 + \gamma_m^2}. \quad (24)$$

The derivation of these equations is given in the Appendix B. Since the right eigenvectors  $\{\mathbf{u}_m\}$  and the left eigenvectors  $\{\mathbf{v}_m\}$  form bi-orthogonal basis sets, the following relationships hold:

$$\mathbf{v}_n^\dagger \cdot \mathbf{u}_m = 0 \quad (m \neq n), \quad (25)$$

$$\mathbf{u}_m^\dagger \cdot \mathbf{u}_m = 1. \quad (26)$$

In this normalization condition, however, it is noted that  $\mathbf{u}_m^T \cdot \mathbf{u}_m (= \mathbf{v}_m^\dagger \cdot \mathbf{u}_m)$  in Eq. (24) is not equal to 1.

### III. COMPUTATIONAL DETAILS

In order to confirm the validity of this approach, we consider the tight-binding model of a one-dimensional semi-infinite chain. We set the number of atomic sites in the subsystem model cluster  $N$  to 40, and the cluster Hamiltonian reads

$$H_{ij} = \alpha \delta_{i,j} - \beta \delta_{i,j-1} - \beta \delta_{i,j+1} \quad (1 \leq i, j \leq 40), \quad (27)$$

where  $\delta_{ij}$  is the Kronecker delta. We employ the values of  $\alpha = 2.0$  and  $\beta = 0.6$  throughout this study. It is noted that the same results are obtained for the scaled energy  $\zeta$

$$\zeta = \frac{E - \alpha}{2\beta}, \quad (28)$$

and the choice of  $\alpha$  and  $\beta$  is arbitrary in this sense.

Since we consider a semi-infinite chain, the self-energy is added only at one end, the 40th site. The self-energy matrix is expressed by

$$\Sigma_{ij}(\epsilon) = \sigma(\epsilon) \delta_{i,40} \delta_{j,40} \quad (1 \leq i, j \leq 40), \quad (29)$$

and the self-energy  $\sigma(\epsilon)$  in the tight-binding model is written analytically<sup>30</sup>

$$\sigma(\epsilon) = \frac{(\alpha - \text{Re}[\epsilon]) - \sqrt{(\alpha - \text{Re}[\epsilon])^2 - 4\beta^2}}{2}. \quad (30)$$

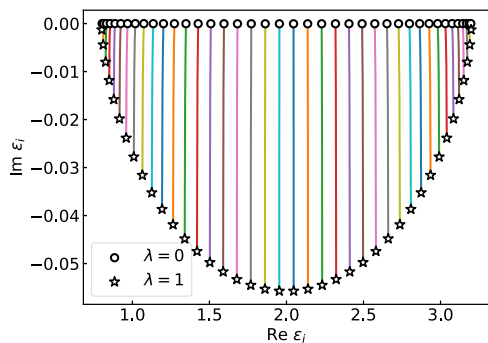


**FIG. 1.** The change in eigenvalues during the adiabatic connection. The circle and star points represent the eigenvalues at  $\lambda = 0$  and  $\lambda = 1$ , respectively.

It is noted that this expression is derived under the outgoing-wave boundary condition. The proposed method can also be applied to the case where non-orthogonal basis sets are used. There,  $\alpha$  and  $\beta$  become matrices, and the self-energy matrix is computed numerically.<sup>31–33</sup>

For calculating the adiabatically connected states, the grid  $\lambda$  is defined as

$$\lambda(l) = \frac{\zeta(l/100) - \zeta(0.0)}{\zeta(1.0) - \zeta(0.0)} \quad (l = 0, 1, \dots, 100), \quad (31)$$

$$\zeta(x) = \frac{1}{1 + \exp(-2(4x - 2))}. \quad (32)$$

The convergence criteria of the iterative scheme in Eq. (15) to Eq. (21) is set to  $1.0 \times 10^{-6}$ .

## IV. RESULTS AND DISCUSSION

### A. Construction of CAP

In this section, the details of the construction are shown. Figure 1 displays the trace of the eigenvalues during the adiabatic connection. The number of lines is 40, corresponding to the size of the cluster Hamiltonian. The circle points at  $\lambda = 0$  lie on the real axis and represent bound states of the cluster Hamiltonian. As the  $\lambda$  value increases, these eigenvalues are continuously connected to the complex plane. Since the star plots at  $\lambda = 1$  have negative imaginary parts, it can be confirmed that the resonance states associated with the bound states of the cluster are indeed obtained.

The structure of the cluster Hamiltonian and the constructed CAP in the tight-binding basis are illustrated in Fig. 2. In this example,  $\overline{\mathbf{W}}^{\text{opt}}$  is obtained as  $\overline{\mathbf{W}}_3$ . It can be seen that both the real and imaginary parts of the constructed CAP are localized near the junction with the bulk solid ( $i = 40$ ). This seems to be a reasonable approximation to the self-energy only added to the 40th site. From the enlarged view of the lower right component of Figs. 2(b) and 2(c), it is clear that the CAP is indeed complex-symmetric.

To verify the validity of the obtained CAP, the DOS was calculated using the complex eigenvalues obtained from the OCM calculation with Eq. (23). The analytical expression for the exact DOS of a semi-infinite chain is<sup>34</sup>

$$\rho(E) = \frac{1}{\pi} \frac{1}{\sqrt{4\beta^2 - (\alpha - E)^2}} \quad (\alpha - 2\beta \leq E \leq \alpha + 2\beta), \quad (33)$$

and the graph is plotted with the solid black line in Fig. 3. In contrast, the DOS of the cluster Hamiltonian is discrete, as in the following equation:

$$\rho(E) = \sum_{m=1}^{40} \delta(E - \omega_m), \quad (34)$$

which is given by setting  $\gamma_m$  to 0 in Eq. (23). In this way, the conventional cluster model cannot reproduce the continuous DOS of the solid due to its finite size.

The DOS curves obtained from the OCM calculations with  $\overline{\mathbf{W}}_1$  and  $\overline{\mathbf{W}}^{\text{opt}}$  are shown as the green and red lines, respectively. It can be seen that both are able to reproduce the exact shape of the other. This can be related to the behavior of Fig. 1. The larger the magnitude of the imaginary part of a complex eigenvalue, the lower and wider the Lorentz function in Eq. (23) becomes. This means that the magnitude of the imaginary part must be small at the band edges and large in the center to reproduce the shape of the exact DOS for the semi-infinite chain, as observed in Fig. 1. While there are some approaches that artificially broaden the discrete DOS to mimic the solid electronic structure,<sup>35,36</sup> the strength of this method is that the optimal width is automatically chosen for each energy level without such artificiality.

On the other hand, when the CAP  $\overline{\mathbf{W}}_1$  is used, the DOS has negative values at the band edges. This is a non-physical behavior and conceptually inappropriate for the OCM calculations in the sense that  $\overline{\mathbf{W}}_1$  cannot completely impose the outgoing-wave boundary condition on the cluster. The reason for this is that the imaginary

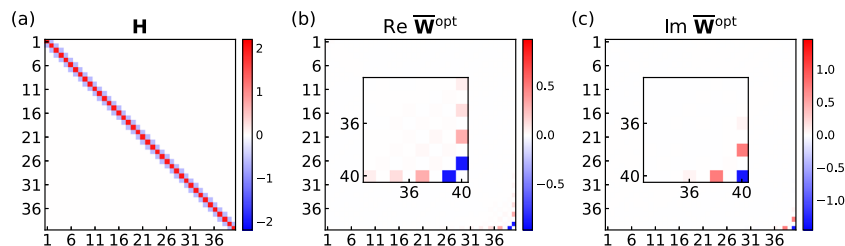


**FIG. 2.** The structure of (a) the cluster Hamiltonian, (b) the real part of the constructed CAP, and (c) its imaginary part are shown. The CAP has values only near the junction with the solid ( $i = 40$ ), and these areas are shown in inset plots.

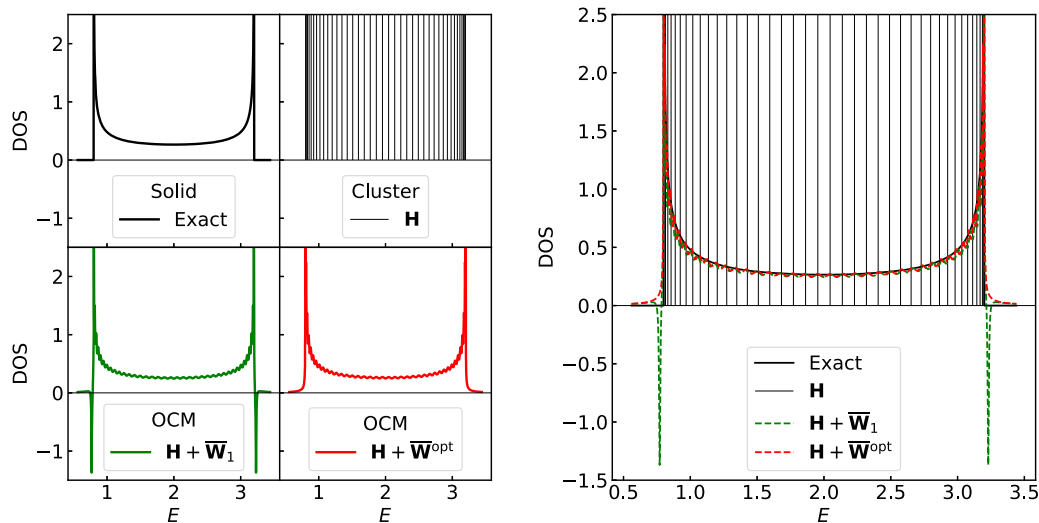


**FIG. 3.** The comparison of the DOS based on the results of OCM calculations. The exact DOS for one-dimensional solid is shown in the solid black line. The thin black line represents the DOS of the cluster calculated by Eq. (23). The green line is obtained from the OCM calculation with the conventional CAP  $\bar{W}_1$ , showing a negative region at the band edge. The CAP constructed by the new method  $\bar{W}^{\text{opt}}$  well reproduces the exact shape (red line).

parts of the eigenvalues near the band edges are positive based on the DOS formula in Eq. (23). This may occur because these imaginary parts are small and are easily affected by symmetrizing the right and left CAPs. Since the newly proposed method determines the CAP  $\bar{W}^{\text{opt}}$  in such a way as to reproduce the target eigenvalues  $\epsilon_1$ , such a problem is not expected to occur. Conversely, the eigenvalues responsible for broadening near the center of the band have large imaginary parts and seem to be less affected by the symmetrization of the CAP.

### B. Newns-Anderson-Grimley model

To demonstrate the applicability of this method, we applied the constructed CAP to calculate the surface adsorption states. Within the category of the tight-binding model for 1D solids, a model describing surface adsorption states has been investigated by Anderson,<sup>37</sup> Newns,<sup>38</sup> and Grimley.<sup>39,40</sup> In this context, the  $N \times N$  Hamiltonian  $\mathbf{H}^{\text{mod}}$  is defined by modifying the Hamiltonian in Eq. (27) as follows:

$$\mathbf{H}^{\text{mod}} = \left[ \begin{array}{c|ccc} \alpha_1 & -\eta\beta & & \mathbf{0} \\ \hline -\eta\beta & \alpha & -\beta & \\ & -\beta & \alpha & \\ & & & \ddots \\ \mathbf{0} & & & \alpha & -\beta \\ & & & -\beta & \alpha \end{array} \right]. \quad (35)$$

Two real parameters,  $\eta$  and  $\alpha_1$ , are introduced to describe the surface state.  $\eta$  modulates the strength of interaction between the

adsorbed and substrate-edge atoms, while  $\alpha_1$  specifies the energy level of the adsorbed atom. The number and types of localized surface states are determined by these two parameters. Newns presented the phase diagram as shown in Fig. 4.<sup>38</sup> In this paper, this model is referred to as the Newns model.

The Newns model can express various surface states by varying the two parameters. Constructing the CAP with the iterative scheme each time these parameters are changed is considered the

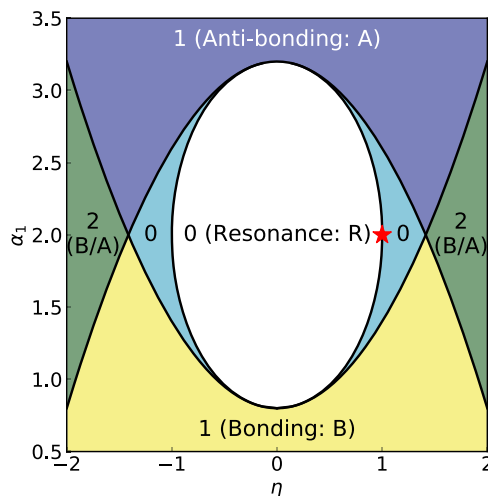


**FIG. 4.** The phase diagram of the Newns model is illustrated with respect to two parameters  $\eta$  and  $\alpha_1$  [see Eq. (35)]. The numbers and types of bound states outside the band edges are shown. The characters B and A mean the existence of bonding and antibonding surface states, respectively. In the central white region, a resonance state appears. The red star ( $\eta = 1.0, \alpha_1 = 2.0$ ) corresponds to the parameter of pure solid.

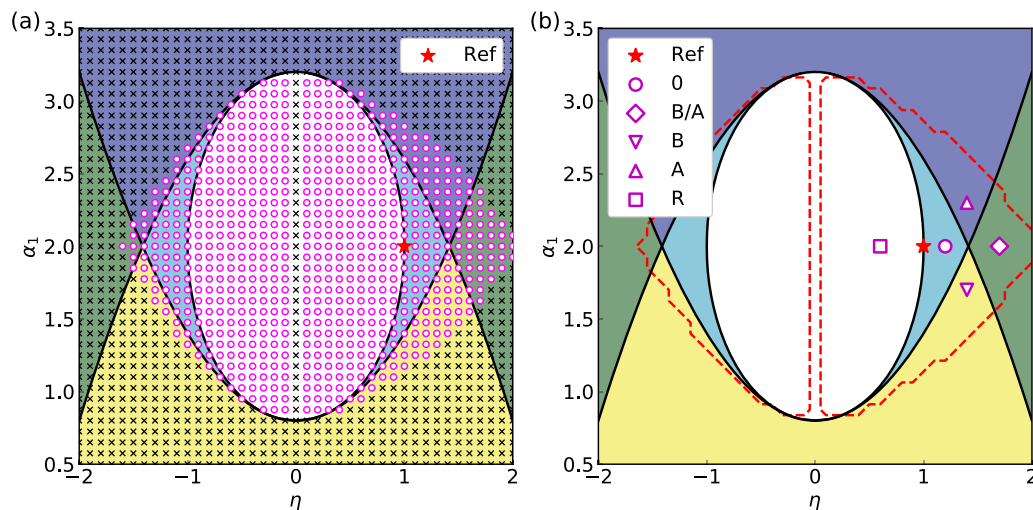


**FIG. 5.** (a) Regions where all eigenvalues have negative imaginary parts are indicated by circles. (b) The parameter sets that reproduce the five different surface states of the Newns model were selected within the region in (a).

most accurate approach. However, this approach is computationally expensive when actually applied to quantum chemical calculations. Therefore, in this study, we explored the possibility of reusing the CAP constructed at one reference point. A pure solid, represented by  $\eta = 1.0$  and  $\alpha_1 = 2.0$ , where the CAP works effectively in the previous section, is taken as the reference point and shown as the red star in Fig. 4. Namely, the following OCM calculation is performed to examine whether the surface states in the Newns model are reproduced correctly

$$\bar{\mathbf{W}}^{\text{ref}} \equiv \bar{\mathbf{W}}^{\text{opt}}(\eta = 1.0, \alpha_1 = 2.0), \quad (36)$$

$$[\mathbf{H}^{\text{mod}}(\eta, \alpha_1) + \bar{\mathbf{W}}^{\text{ref}}] \mathbf{u}_m^{\text{mod}} = (\omega_m^{\text{mod}} - i\gamma_m^{\text{mod}}) \mathbf{u}_m^{\text{mod}}. \quad (37)$$

To explore various parameters, OCM calculations with Eq. (37) were performed by changing their values by  $\Delta\eta = 0.1$  and  $\Delta\alpha_1 = 0.075$  steps in the range of Fig. 4. For each point, 40 complex eigenvalues are obtained, and the regions where their imaginary parts are all negative are plotted as circles in Fig. 5(a). This clarifies whether the CAP optimized at the reference point correctly imposes the outgoing-wave boundary condition on the clusters with modified surfaces. We can see that  $\bar{\mathbf{W}}^{\text{ref}}$  can be reused for parameter sets that do not have large perturbations from the reference point. Furthermore, the circles overlap in all five regions, representing the five different surface conditions in the Newns model. It is expected that each of these states can be commonly calculated with  $\bar{\mathbf{W}}^{\text{ref}}$ .

To investigate this point, we selected five parameter sets  $(\eta, \alpha_1)$  with different surface conditions and calculated the DOS and the PDOS projected onto the adsorbed atom  $\rho_{11}(E)$ . The values of the parameters are shown in Table I, and each point is also illustrated in Fig. 5(b).

**TABLE I.** The set of parameters to reproduce five surface conditions.

Surface states	$\eta$	$\alpha_1$
0	1.2	2.0
B/A	1.7	2.0
B	1.4	1.7
A	1.4	2.3
R	0.6	2.0

DOS and PDOS curves obtained by OCM calculations are shown in Fig. 6 together with the exact ones. In this figure, the exact DOS and PDOS are calculated by the following equations:<sup>41</sup>

$$\mathbf{H}_{\Sigma}(z) \equiv \mathbf{H}^{\text{mod}} + \Sigma(z), \quad (38)$$

$$\mathbf{G}_{\Sigma}(z) \equiv (z\mathbf{I} - \mathbf{H}_{\Sigma}(z))^{-1}, \quad (39)$$

$$\rho(E) = -\frac{1}{N} \frac{1}{\pi} \text{Tr} [\text{Im} \mathbf{G}_{\Sigma}(E + i\delta)], \quad (40)$$

$$\rho_{11}(E) = -\frac{1}{\pi} [\text{Im} \mathbf{G}_{\Sigma}(E + i\delta)]_{11}. \quad (41)$$

It can be seen that, for any surface conditions, both the DOS and PDOS obtained from the OCM calculation reproduce the exact solution well. For example, in the region of zero surface state,  $\eta$  and  $\alpha_1$  are close to the values in the pure solid. Therefore, the adsorbed atom contributes to the solid electronic band, similar to the other atoms in the solid. In fact, the PDOS has a rather flat shape within the band region, and the OCM result mimics the shape well despite the linear combination of the Lorentz functions. In regions B/A, B and A, bound states appear due to two factors. The first is the

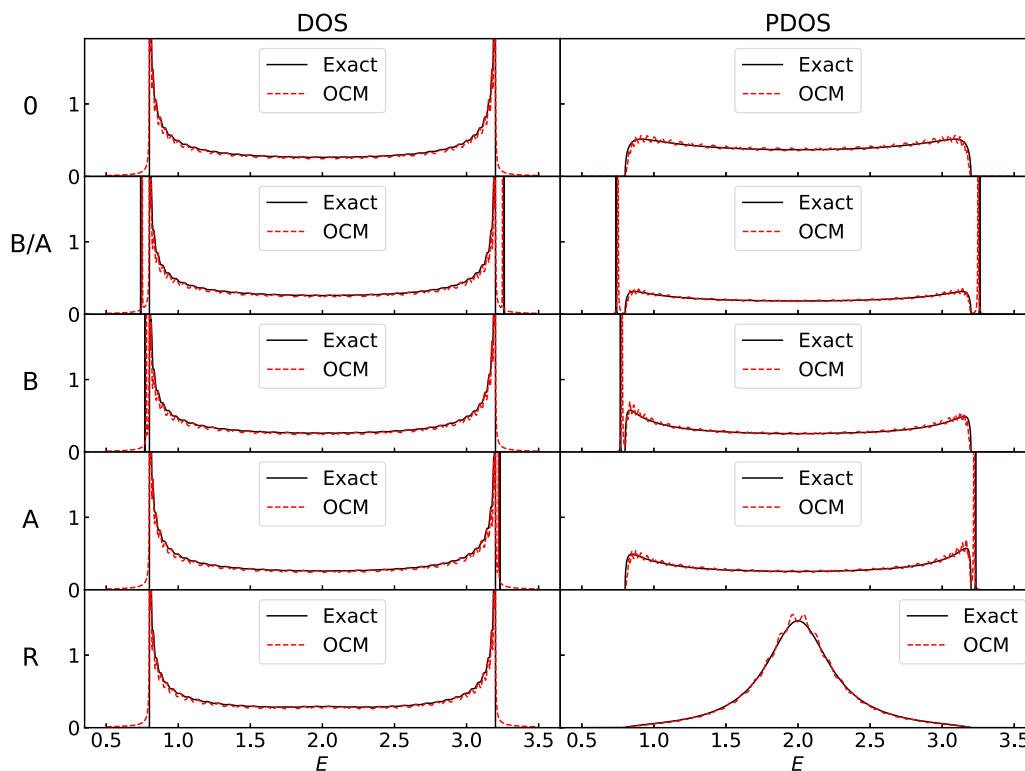


**FIG. 6.** The DOS and PDOS are calculated for the five parameters in Fig. 5(b). The exact curves are shown in black, and the results from OCM calculations are expressed by the red dashed lines. We introduce the imaginary shift  $\delta = 1.0 \times 10^{-5}$  in Eqs. (40) and (41) to visualize the sharp peaks in bonding and anti-bonding states.

isolation of the energy level of the adsorbed atom from the solid band, resulting from  $\alpha_1$  moving up or down relative to  $\alpha$  in the substrate atoms. Second, the coupling  $\eta$  between the adsorbed atom and the substrate-edge atom is strong, resulting in a large energy splitting. Therefore, the sharp peaks in the DOS representing bound states must necessarily be associated with the PDOS of the adsorbed atom. Both exact and OCM curves show that the sharp peak in the DOS is actually attributed to the PDOS of the adsorbed atom. It is important to note that the B/A states and solid electronic structure can be described in a unified framework. Although OCM primarily aims to model the latter with resonance states, the B/A states can be expressed as infinite-lifetime resonance states. Resonance states are realized when the coupling  $\eta$  is weak, i.e., the adsorbed atom and the substrate-edge atom interact weakly. It can be seen that the bell-shaped PDOS shape can also be reproduced by the OCM calculation. In this way, it is shown that the five typical surface states of the Newns model can be obtained through the OCM calculations, even when the CAP is reused.

Concerning the transferability of the current CAP, the explanation might be attributed to the localized nature of the self-energy in Eq. (29) and the resulting CAP matrix in Fig. 2. In a previous study that employed Henderson's CAP for more realistic calculations,<sup>42</sup> it was pointed out that including the explicit electrode region, in addition to the cluster region, was important. When conducting OCM

calculations with the proposed CAP, we anticipate that the explicit electrode region should extend at least to the area where the matrix elements of the CAP have values. Since the size is approximately ten in the current result (Fig. 2), we can ensure that the size of the total system ( $N = 40$ ) is sufficiently large. However, it is essential to verify whether such locality holds for practical calculations, and care must be taken in selecting the system size.

Finally, the orbital coefficients are illustrated for the case where bonding and antibonding (B/A) surface states emerge. The decomposition of the DOS into Lorentz functions in Fig. 7(a) indicates that only one state with energy  $\epsilon_1$  is associated with the bonding state and that with energy  $\epsilon_{40}$  is linked to the antibonding state. These two states exist outside the shaded area, indicating the solid band, which possesses the characteristics of bound states in the Newns chemisorption model. Figure 7(b) illustrates the real part of the orbital coefficients for these states, focusing on the vicinity of the surface. For  $\mathbf{v}_1$ , the coefficients of the first site (adsorbed atom) and the second site (substrate-edge atom) are in the same phase, whereas for  $\mathbf{v}_{40}$ , they are in the opposite phase. This can be understood by the interaction between the energy level of the adsorbed atom and the solid band, similar to the mixing of two orbitals producing bonding and antibonding orbitals.

It is noted that the real parts of the right and left eigenvectors coincide because the CAP is symmetrized by the present

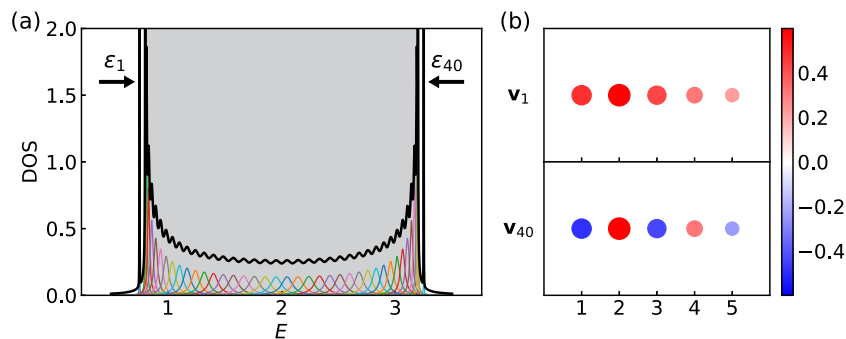


**FIG. 7.** (a) The DOS of the B/A state and the Lorentz functions that make up it are shown. The region where the energy takes values from  $\alpha - 2\beta$  to  $\alpha + 2\beta$  is shaded, which corresponds to the solid band. Two bound states with energies  $\epsilon_1$  and  $\epsilon_{40}$  exist outside the band edges. (b) The real part of the orbital coefficients for the two bound states is illustrated only near the surface ( $i = 1$ ).

method. This allows us to treat the real part of the orbital coefficients in OCM calculations as those in ordinary quantum chemical calculations.

## V. CONCLUSION

In this study, we developed a new method for constructing the CAP reproducing the environment in solids and applied it to OCM calculations. As a result, the calculation of the tight-binding model for a 1D semi-infinite chain was carried out using a finite-size cluster, and the exact solution was well reproduced for the DOS and PDOS.

The feature of the obtained CAP is that it contains no parameters and is free from complex variational principles such as the  $\eta$ -trajectory method. An additional advantage is that the CAP contains information on all orbitals constituting a solid band, so it can be referred to as a “band-specific” CAP, not a “state-specific” one. There is also the physical support that can be obtained as an approximation for the self-energy in the surface Green’s function theory. With the iterative scheme proposed in this study, we have succeeded in constructing a symmetrized CAP that can reproduce the solid-state DOS and PDOS. Symmetrization of the CAP not only brings cost savings in matrix operations in quantum chemical calculations envisioned for the future but also provides interpretability for the orbital coefficients, as the real parts of the right and left eigenvectors coincide. Furthermore, for symmetric CAPs, it is possible to obtain a spatial representation that reproduces the matrix representation. We believe that this real-space CAP can be used for calculations with basis sets different from those used in the optimization and can be extended to the calculations of higher-dimensional materials.

On the other hand, the sequential optimization of the CAP for each perturbation to the cluster Hamiltonian, such as surface modification and structural change, is computationally expensive. Therefore, we tested whether the approach of reusing the CAP once constructed in the reference cluster is appropriate for describing surface states in the Newns model. When the reference point is taken to be a pure solid, it is confirmed that all five types of surface states in the Newns model can be adequately described. From this result, it can be said that the optimization of the CAP can be greatly reduced if appropriate reference points are taken. This is an important property

for structural optimization calculations of surface adsorption states and for discussions of the effects of local substitution on periodic materials.

We demonstrated the new approach with a simple model but would like to extend it to real systems in the future. To do so, we need to extend the method to cases where non-orthogonal basis sets are used. We also have to consider the iterative construction of Fock matrices due to the two-electron terms that appear in quantum chemical calculations. We hope to address these tasks and establish the method, which has different strengths compared to ordinary cluster models and band calculations with supercells.

## ACKNOWLEDGMENTS

K.I. acknowledges the grant-in-aid for the Japan Society for Promotion of Science (JSPS) Fellows. This work was supported by JSPS KAKENHI (Grant Nos. JP21J21500 and JP23H01922). Theoretical computations were partly performed using the Research Center for Computational Science, Okazaki, Japan (Project No. 21-IMS-C021).

## AUTHOR DECLARATIONS

### Conflict of Interest

The authors have no conflicts to disclose.

### Author Contributions

**Kosuke Imamura:** Funding acquisition (equal); Investigation (equal); Writing – original draft (equal). **Tomokazu Yasuike:** Supervision (equal). **Hirofumi Sato:** Conceptualization (equal); Funding acquisition (equal); Project administration (equal); Supervision (equal); Writing – review & editing (equal).

### DATA AVAILABILITY

The data that support the findings of this study are available from the corresponding author upon reasonable request.

## APPENDIX A: THE EXPRESSION OF THE GREEN'S MATRIX IN THE BI-ORTHOGONAL BASIS SETS

We define the Hamiltonian  $\mathbf{H}'$  as the sum of the cluster Hamiltonian  $\mathbf{H}$  and the energy-independent CAP  $\mathbf{W}$ . The eigenvalue equations are shown below:

$$\mathbf{H}' \equiv \mathbf{H} + \mathbf{W}, \quad (\text{A1})$$

$$\mathbf{H}' \mathbf{u}_m = \epsilon_m \mathbf{u}_m, \quad (\text{A2})$$

$$\mathbf{v}_m^\dagger \mathbf{H}' = \epsilon_m \mathbf{v}_m^\dagger. \quad (\text{A3})$$

The definition of the Green's matrix is

$$\mathbf{G}(z) = (z\mathbf{I} - \mathbf{H}')^{-1}, \quad (\text{A4})$$

where  $z$  is equal to  $E + i\delta$  ( $\delta > 0$ ).

The Green's matrix can be expanded with the right eigenvectors  $\{\mathbf{u}_m\}$  as follows:

$$\mathbf{G}(z) = (\mathbf{u}_1, \mathbf{u}_2, \dots, \mathbf{u}_N) \begin{pmatrix} D_{11} & D_{12} & \cdots & D_{1N} \\ D_{21} & D_{22} & \cdots & D_{2N} \\ \vdots & \vdots & \ddots & \vdots \\ D_{N1} & D_{N2} & \cdots & D_{NN} \end{pmatrix}. \quad (\text{A5})$$

From the definition of  $\mathbf{G}(z)$ , we obtain the following relationship:

$$\begin{aligned} (z\mathbf{I} - \mathbf{H}')\mathbf{G}(z) &= (z\mathbf{I} - \mathbf{H}')(\mathbf{u}_1, \dots, \mathbf{u}_N)\mathbf{D}(z), \\ &= (\mathbf{u}_1, \dots, \mathbf{u}_N) \begin{pmatrix} z - \epsilon_1 & & & 0 \\ & \ddots & & \\ & & \ddots & \\ 0 & & & z - \epsilon_N \end{pmatrix} \mathbf{D}(z) = \mathbf{I}. \end{aligned} \quad (\text{A6})$$

By multiplying the matrix  $(\mathbf{v}_1^\dagger, \mathbf{v}_2^\dagger, \dots, \mathbf{v}_N^\dagger)^T$  from the left and using the bi-orthogonal relationship in Eqs. (25) and (26), the following equation holds:

$$\begin{pmatrix} \mathbf{v}_1^\dagger \cdot \mathbf{u}_1 & & & 0 \\ & \ddots & & \\ 0 & & & \mathbf{v}_N^\dagger \cdot \mathbf{u}_N \end{pmatrix} \begin{pmatrix} z - \epsilon_1 & & & 0 \\ & \ddots & & \\ & & \ddots & \\ 0 & & & z - \epsilon_N \end{pmatrix} \mathbf{D}(z) = \begin{pmatrix} \mathbf{v}_1^\dagger \\ \vdots \\ \mathbf{v}_N^\dagger \end{pmatrix}, \quad (\text{A7})$$

and the matrix  $\mathbf{D}(z)$  is expressed by

$$\mathbf{D}(z) = \begin{pmatrix} \frac{1}{\mathbf{v}_1^\dagger \cdot \mathbf{u}_1 (z - \epsilon_1)} & & & 0 \\ & \ddots & & \\ 0 & & & \frac{1}{\mathbf{v}_N^\dagger \cdot \mathbf{u}_N (z - \epsilon_N)} \end{pmatrix} \begin{pmatrix} \mathbf{v}_1^\dagger \\ \vdots \\ \mathbf{v}_N^\dagger \end{pmatrix}. \quad (\text{A8})$$

The expression of Green's matrix is thus obtained as

$$\begin{aligned} \mathbf{G}(z) &= (\mathbf{u}_1, \mathbf{u}_2, \dots, \mathbf{u}_N)\mathbf{D}(z), \\ &= \sum_{m=1}^N \frac{1}{z - \epsilon_m} \frac{\mathbf{u}_m \mathbf{v}_m^\dagger}{\mathbf{v}_m^\dagger \cdot \mathbf{u}_m}. \end{aligned} \quad (\text{A9})$$

## APPENDIX B: THE EXPRESSIONS OF THE DOS AND PDOS IN OCM

The definitions of DOS and PDOS are given by<sup>41</sup>

$$\rho(E) = -\frac{1}{N} \frac{1}{\pi} \lim_{\delta \rightarrow +0} \text{Im} [\text{Tr} \mathbf{G}(z)], \quad (\text{B1})$$

$$\rho_{ii}(E) = -\frac{1}{\pi} \lim_{\delta \rightarrow +0} \text{Im} G_{ii}(z). \quad (\text{B2})$$

By using the following equation,

$$\begin{aligned} \text{Tr} [\mathbf{u}_m \mathbf{v}_m^\dagger] &= \text{tr} \begin{pmatrix} u_{1m} v_{m1}^* & u_{1m} v_{m2}^* & \cdots & u_{1m} v_{mN}^* \\ u_{2m} v_{m1}^* & u_{2m} v_{m2}^* & \cdots & u_{2m} v_{mN}^* \\ \vdots & \vdots & \ddots & \vdots \\ u_{Nm} v_{m1}^* & u_{Nm} v_{m2}^* & \cdots & u_{Nm} v_{mN}^* \end{pmatrix}, \\ &= \sum_{i=1}^N u_{im} v_{mi}^* = \mathbf{v}_m^\dagger \cdot \mathbf{u}_m, \end{aligned} \quad (\text{B3})$$

the DOS expression is written as

$$\begin{aligned} \rho(E) &= -\frac{1}{N} \frac{1}{\pi} \lim_{\delta \rightarrow +0} \text{Im} \sum_{m=1}^N \frac{1}{z - \epsilon_m} \\ &= -\frac{1}{N} \frac{1}{\pi} \lim_{\delta \rightarrow +0} \text{Im} \sum_{m=1}^N \frac{1}{(E - \omega_m) + i(\delta + \gamma_m)} \\ &= \frac{1}{N} \frac{1}{\pi} \lim_{\delta \rightarrow +0} \sum_{m=1}^N \frac{\gamma_m + \delta}{(E - \omega_m)^2 + (\delta + \gamma_m)^2} \\ &= \frac{1}{N} \frac{1}{\pi} \sum_{m=1}^N \frac{\gamma_m}{(E - \omega_m)^2 + \gamma_m^2}. \end{aligned} \quad (\text{B4})$$

A similar transformation of Eq. (B2) yields the expression for the PDOS

$$\begin{aligned} \rho_{ii}(E) &= -\frac{1}{\pi} \lim_{\delta \rightarrow +0} \text{Im} \sum_{m=1}^N \frac{1}{z - \epsilon_m} \frac{(\mathbf{u}_m \mathbf{v}_m^\dagger)_{ii}}{\mathbf{v}_m^\dagger \cdot \mathbf{u}_m} \\ &= -\frac{1}{\pi} \lim_{\delta \rightarrow +0} \text{Im} \sum_{m=1}^N \frac{1}{(E - \omega_m) + i(\delta + \gamma_m)} \frac{(\mathbf{u}_m \mathbf{v}_m^\dagger)_{ii}}{\mathbf{v}_m^\dagger \cdot \mathbf{u}_m} \\ &= -\frac{1}{\pi} \lim_{\delta \rightarrow +0} \sum_{m=1}^N \frac{1}{(E - \omega_m)^2 + (\delta + \gamma_m)^2}, \\ &\quad \times \text{Im} \left[ \frac{(\mathbf{u}_m \mathbf{v}_m^\dagger)_{ii}}{\mathbf{v}_m^\dagger \cdot \mathbf{u}_m} \{E - \omega_m - i(\delta + \gamma_m)\} \right] \\ &= -\frac{1}{\pi} \sum_{m=1}^N \frac{\text{Im} \left[ \frac{(\mathbf{u}_m \mathbf{v}_m^\dagger)_{ii}}{\mathbf{v}_m^\dagger \cdot \mathbf{u}_m} (E - \omega_m - i\gamma_m) \right]}{(E - \omega_m)^2 + \gamma_m^2}. \end{aligned} \quad (\text{B5})$$

## REFERENCES

- <sup>1</sup>P. Huang and E. A. Carter, *Annu. Rev. Phys. Chem.* **59**, 261 (2008).
- <sup>2</sup>F. Libisch, C. Huang, and E. A. Carter, *Acc. Chem. Res.* **47**, 2768 (2014).
- <sup>3</sup>C. Freysoldt *et al.*, *Rev. Mod. Phys.* **86**, 253 (2014).
- <sup>4</sup>O. T. Hofmann, E. Zojer, L. Hörmann, A. Jeindl, and R. J. Maurer, *Phys. Chem. Chem. Phys.* **23**, 8132 (2021).
- <sup>5</sup>V. Georgakilas *et al.*, *Chem. Rev.* **112**, 6156 (2012).
- <sup>6</sup>H. Grimmeiss, *Annu. Rev. Mater. Sci.* **7**, 341 (1977).
- <sup>7</sup>H. Evjen, *Phys. Rev.* **39**, 675 (1932).
- <sup>8</sup>M. A. Nygren and L. G. Pettersson, *J. Phys. Chem.* **100**, 1874 (1996).
- <sup>9</sup>M. Matsui and S. Sakaki, *J. Phys. Chem. C* **121**, 20242 (2017).
- <sup>10</sup>G. A. Bramley, O. T. Beynon, P. V. Stishenko, and A. J. Logsdail, *Phys. Chem. Chem. Phys.* **25**, 6562 (2023).
- <sup>11</sup>Y. Lu *et al.*, *Phys. Chem. Chem. Phys.* **25**, 21816 (2023).
- <sup>12</sup>Q. Sun and G. K.-L. Chan, *Acc. Chem. Res.* **49**, 2705 (2016).
- <sup>13</sup>L. O. Jones, M. A. Mosquera, G. C. Schatz, and M. A. Ratner, *J. Am. Chem. Soc.* **142**, 3281 (2020).
- <sup>14</sup>T. Yasuike and K. Nobusada, *Phys. Rev. B* **76**, 235401 (2007).
- <sup>15</sup>T. Yasuike and K. Nobusada, *Chem. Phys. Lett.* **457**, 241 (2008).
- <sup>16</sup>T. Yasuike and K. Nobusada, *Phys. Rev. B* **80**, 035430 (2009).
- <sup>17</sup>T. Yasuike and K. Nobusada, *Phys. Rev. B* **84**, 245408 (2011).
- <sup>18</sup>A. J. F. Siegert, *Phys. Rev.* **56**, 750 (1939).
- <sup>19</sup>N. Moiseyev, *Non-Hermitian Quantum Mechanics* (Cambridge University Press, 2011).
- <sup>20</sup>D. R. Jones and A. Troisi, *Phys. Chem. Chem. Phys.* **12**, 4625 (2010).
- <sup>21</sup>G. Fratesi, C. Motta, M. I. Trioni, G. P. Brivio, and D. Sánchez-Portal, *J. Phys. Chem. C* **118**, 8775 (2014).
- <sup>22</sup>D. Sulzer, S. Iuchi, and K. Yasuda, *J. Chem. Theory Comput.* **12**, 3074 (2016).
- <sup>23</sup>R. Santra, L. S. Cederbaum, and H.-D. Meyer, *Chem. Phys. Lett.* **303**, 413 (1999).
- <sup>24</sup>T. Sommerfeld and M. Ehara, *J. Chem. Theory Comput.* **11**, 4627 (2015).
- <sup>25</sup>D. E. Manolopoulos, *J. Chem. Phys.* **117**, 9552 (2002).
- <sup>26</sup>N. Moiseyev, P. R. Certain, and F. Weinhold, *Mol. Phys.* **36**, 1613 (1978).
- <sup>27</sup>Y. Sajeev, V. Vysotskiy, L. S. Cederbaum, and N. Moiseyev, *J. Chem. Phys.* **131**, 211102 (2009).
- <sup>28</sup>T.-C. Jagau, K. B. Bravaya, and A. I. Krylov, *Annu. Rev. Phys. Chem.* **68**, 525 (2017).
- <sup>29</sup>T. M. Henderson, G. Fagas, E. Hyde, and J. C. Greer, *J. Chem. Phys.* **125**, 244104 (2006).
- <sup>30</sup>G. Cuniberti, G. Fagas, and K. Richter, *Chem. Phys.* **281**, 465 (2002).
- <sup>31</sup>M. P. L. Sancho, J. M. L. Sancho, and J. Rubio, *J. Phys. F: Met. Phys.* **15**, 851 (1985).
- <sup>32</sup>A. Umerski, *Phys. Rev. B* **55**, 5266 (1997).
- <sup>33</sup>M. G. Reuter, T. Seideman, and M. A. Ratner, *Phys. Rev. B* **83**, 085412 (2011).
- <sup>34</sup>R. A. Santen, *Theoretical Heterogeneous Catalysis* (World Scientific, 1991).
- <sup>35</sup>C. Y. Yang, K. H. Johnson, D. R. Salahub, J. Kaspar, and R. P. Messmer, *Phys. Rev. B* **24**, 5673 (1981).
- <sup>36</sup>K. Lee, J. Callaway, and S. Dhar, *Phys. Rev. B* **30**, 1724 (1984).
- <sup>37</sup>P. W. Anderson, *Phys. Rev.* **124**, 41 (1961).
- <sup>38</sup>D. M. Newns, *Phys. Rev.* **178**, 1123 (1969).
- <sup>39</sup>T. B. Grimley, *Proc. Phys. Soc.* **72**, 103 (1958).
- <sup>40</sup>T. B. Grimley, *Proc. Phys. Soc.* **90**, 751 (1967).
- <sup>41</sup>S. G. Davison and K. W. Sulston, *Green-Function Theory of Chemisorption* (Springer Science and Business Media, 2006).
- <sup>42</sup>M. Szeplieniec, I. Yeriskin, and J. C. Greer, *J. Chem. Phys.* **138**, 144105 (2013).